Non-central camera refraction calibration using coplanarity constraints for the photogrammetric system with optical sphere cover

WENJUAN YANG,[1,3] XUHUI ZHANG,[1,3,*] HONGWEI MA,[1,3] GUANGMING ZHANG,[2] AND GANG YANG[4]

[1] *School of Mechanical Engineering, Xi'an University of Science and Technology, No.58, Yanta Road, Xi'an 710054, China*
[2] *Electronic and Ultrasonic Engineering Group, General Engineering Research Institute, Liverpool John Moores University, UK*
[3] *Shaanxi Key Laboratory of Mine Electromechanical Equipment Intelligent Monitoring in Shaanxi, No.58, Yanta Road, Xi'an 710054, China*
[4] *MARCO automatic control system development co. LTD, No. 20, Fenghui South Road, Xi'an 710054, China*
**Corresponding author: zhangxh@xust.edu.cn*

Received XX Month XXXX; revised XX Month, XXXX; accepted XX Month XXXX; posted XX Month XXXX (Doc. ID XXXXX); published XX Month XXXX

The optical sphere cover is widely used in photogrammetric systems to protect the optical system from an outside environment. However, the spherical refractive can result in severe non-linear distortion and make the measurement system imprecise and unreliable. This letter presents a novel refractive calibration method for the non-central camera with an optical sphere cover. A geometrical model is established with coplanarity constraints, which considered explicitly the sphere refractive and can preserve an equivalent collinearity relation. Moreover, a calibration method was proposed to estimate the relative orientation parameters. Both numerical and experimental results demonstrate that the methods are effective and robustness.

http://dx.doi.org/10.1364/OL.99.099999

Camera calibration is a hot issue in computer vision [1-3], and the well-known perspective camera models [4-6] are remarkably successful examples for photogrammetric systems. Underground photogrammetric systems normally work in the harsh environment such as dust, water mist, and so on. In coal mining, spherical or flat optical covers are widely used to protect the camera from severe environment, resulting in image distortion. Due to that the refraction effects caused by these covers cannot be simply modeled as perspective camera model, modeling and calibrating such a non-central photogrammetric system remains a challenging problem. The non-central camera calibration has been paid great attention recently, especially in underwater photogrammetric systems [7-9]. The nonlinear distortion caused by the hemisphere and planar refraction in underwater photogrammetry is discussed, however no solution to this problem is presented in [10]. The refraction effects are calibrated using an approximated model such as focal length adjustment or lens radial distortion [11, 12] in the early underwater vision, which usually result in calibration errors. It has also been demonstrated in [13] that refractive effects cannot be well compensated by using a single viewpoint (SVP) model in underwater camera calibration. An underwater camera calibration model with explicit incorporation of refraction was proposed in [14], but it needs a good initial estimate for the housing parameters. A stereo camera geometrical model with single-layer waterproof housing was developed in [15, 16]. A calibration method based on axis estimation was presented for multi-layer flat refractive in [17]. With the dispersion of light taken into consideration, calibration accuracy was improved in [18] by extend the work in [17]. The calibration was performed through the established pixel correspondences in the underwater stereo camera system and the sparse bundle adjustment was applied to refines the calibration results in [19]. The above calibration models are for the camera with a flat optical cover. The nonlinear distortion of the camera with a spherical shield is more severe, which has a great influence on the application of accurate measurement in coal mining. However, there is no effective way to solve this problem. Fig. 1 shows a commercial camera from Marco, which has been widely used in coal mine automation. The camera is installed inside an explosion-proof shell and images are collected through a spherical window.

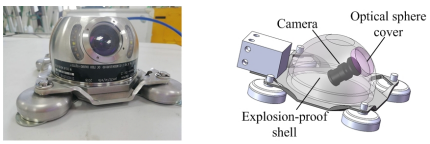

Fig. 1. Camera with an optical sphere cover.

A camera with an optical sphere cover forms a non-central camera imaging system. As shown in Fig. 2(a), the incoming ray v_2,

the normal $\mathbf{m}_1$ of exterior interface and the refracted ray v_1 lie on the same plane $\boldsymbol{\pi}$ according to the Snell's law. Since the normal $\mathbf{m}_2$ of interior interface intersects with $\mathbf{m}_1$ and v_1 at the same time, the normal $\mathbf{m}_2$ lie on the same plane $\boldsymbol{\pi}$. The entire light-path including the given camera ray v_0, v_1, v_2 and the axis $\mathbf{m}_0$, $\mathbf{m}_1$ and $\mathbf{m}_2$ should located on the same plane $\boldsymbol{\pi}$ by induction. The light-path for each 3D space point will form a refractive plane like this, and all refractive planes in such a system actually correspond to the unified axis $\mathbf{m}_0$ that pass through the sphere center $\mathbf{o}$ and the camera center $\mathbf{c}$. It is not only suitable for the case when the camera optical axis is parallel to the axis $\mathbf{m}_0$, but also suitable for general situation when the camera optical axis is not parallel to the axis $\mathbf{m}_0$. The unified axis is named as $\mathbf{m}_0$ in this letter. Hence, a geometrical model is established on the plane of refraction (POR) as shown in Fig. 2(b), (c).

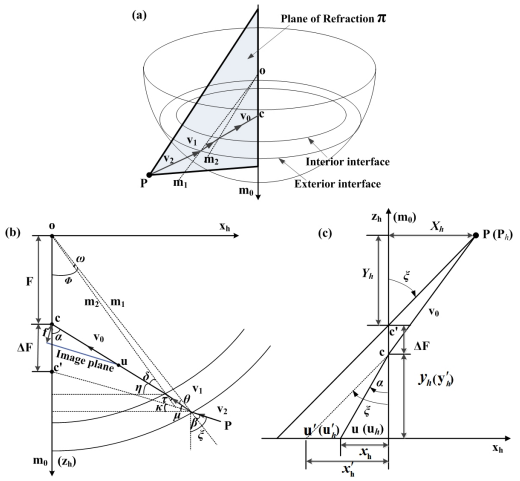

Fig. 2. The geometrical model. (a)Schematic of POR, (b)Projection geometry on POR, (c)Equivalent collinearity relation on POR.

The geometrical model shown in Fig. 2(b) is with the following parameters: β, θ are the incidence angle and refraction angle at exterior interface; τ, δ are the incidence angle and refraction angle at interior interface; α, the angle between the axis $\mathbf{m}_0$ and the camera ray v_0; ω, the angle between the normal $\mathbf{m}_1$ and normal $\mathbf{m}_2$; Φ, the angle between the axis $\mathbf{m}_0$ and the normal $\mathbf{m}_1$; η, μ and κ are the angle between the camera ray v_0, v_1, v_2 and the orthogonal axis $\mathbf{x}_h$, respectively; ξ, the angle between the axis $\mathbf{m}_0$ and the camera ray v_2; f, the focal length; F, the distance from the camera center $\mathbf{c}$ to the sphere center $\mathbf{o}$; ΔF, the offset distance from $\mathbf{c}$ to $\mathbf{c}'$, here $\mathbf{c}'$ is the intersection of v_2 and $\mathbf{m}_0$; R_1, the external radius of the sphere; R_2, the inside radius of the sphere; n, the refractive index of the sphere cover; d, the thickness of the sphere cover, $d=R_1-R_2$. Among which, R_1, R_2 are known parameters of sphere cover. Therefore, once α and F are given, the other angles of $\delta, \beta, \theta, \tau, \omega, \Phi, \mu, \eta, \kappa$ and ξ can be calculated with the following relation

$$\begin{aligned}&\frac{R_2}{\sin(\pi-\alpha)}=\frac{\mathrm{F}}{\sin\delta},\frac{R_1}{\sin(\pi-\tau)}=\frac{R_2}{\sin\theta},\sin\beta=n\sin\theta,\\&\eta=\pi/2-\alpha,\kappa=\pi/2-\Phi-\beta,\xi=\Phi+\beta,\sin\delta=n\sin\tau,\\&\omega=\tau-\theta,\Phi=\alpha-\delta+\omega,\mu=\pi/2-\Phi-\theta\end{aligned}\qquad(1)$$

Assuming that $\mathbf{u}=(x, y)$ is the image coordinate, $\mathbf{v}_0=[x, y, f]^T$ is the direction vector of camera ray v_0. Whereas α can be computed by $\cos\alpha=\mathbf{m}_0\mathbf{v}_0/\|\mathbf{v}_0\|$, $\mathbf{m}_0$ needs to be calculated. Assuming that $\mathbf{P}_w(i)=[X_{wi}, Y_{wi}, Z_{wi}]^T$ is the direction vector of $\mathbf{P}_i$ in the object coordinate system, $\mathbf{v}_0(i)$ is the direction vector of camera ray correspond to $\mathbf{P}_w(i)$. $\mathbf{R}$, $\mathbf{T}$ are the rotation matrix and translation vector. The axis estimation of $\mathbf{m}_0$ can be performed with [17]

$$\begin{bmatrix}\left(\mathbf{P}_w(1)^T\otimes\mathbf{v}_0(1)^T\right)&\mathbf{v}_0(1)^T\\\vdots&\vdots\\\left(\mathbf{P}_w(i)^T\otimes\mathbf{v}_0(i)^T\right)&\mathbf{v}_0(i)^T\end{bmatrix}\begin{bmatrix}\mathbf{E}(:)\\\mathbf{s}\end{bmatrix}=0\qquad(2)$$

where $\otimes$ represents the kronecker product; $\mathbf{E}=[\mathbf{m}_0]\mathbf{R}$, $\mathbf{s}=\mathbf{m}_0\times\mathbf{T}$, $[\mathbf{m}_0]$ denotes the 3 × 3 skew-symmetric matrix of the vector $\mathbf{m}_0$. $\mathbf{m}_0$ can be calculated as the left null singular vector of $\mathbf{E}$.

Thus, with calculated α, the other angles of $\delta, \beta, \theta, \tau, \omega, \Phi, \mu, \eta, \kappa$ and ξ on POR are depends on F. Assuming $\mathbf{P}_c=[X_c, Y_c, Z_c]^T=\mathbf{R}\mathbf{P}_w+\mathbf{T}$ is the point $\mathbf{P}$ in the camera coordinate system. Let $[\mathbf{x}_h, \mathbf{z}_h]$ be the orthogonal coordinate system, where $\mathbf{z}_h$ is the direction vector of $\mathbf{m}_0$, and $\mathbf{x}_h=\mathbf{z}_h\times(\mathbf{z}_h\times\mathbf{v}_0)$ is the orthogonal direction. With introduced $\Delta F=(R_1\sin\Phi-R_2\sin(\alpha-\delta))\tan\mu+R_2\sin(\alpha-\delta)\tan\eta-R_1\sin\Phi\tan\kappa$, as shown in Fig. 2(c), set $\mathbf{P}_h=(X_h, Y_h)$ as the projection of the vector $\mathbf{c}'\mathbf{P}$ along $\mathbf{x}_h$ and $\mathbf{z}_h$,

$$\mathbf{P}_h=\begin{bmatrix}X_h\\Y_h\end{bmatrix}=\begin{bmatrix}\mathbf{x}_h\\\mathbf{z}_h\end{bmatrix}\begin{bmatrix}X_c&Y_c&Z_c\end{bmatrix}^T-\begin{bmatrix}0\\\Delta F\end{bmatrix}\qquad(3)$$

Let $\mathbf{u}_h=(x_h, y_h)$ be the projection of the vector $\mathbf{cu}$ along $\mathbf{x}_h$ and $\mathbf{z}_h$. With the auxiliary line $\mathbf{cu}'$ that is parallel to the $\mathbf{c}'\mathbf{P}$, set $\mathbf{u}'_h=(x'_h, y'_h)$ as the projection of the vector $\mathbf{cu}'$ along $\mathbf{x}_h$ and $\mathbf{z}_h$,

$$\mathbf{u}_h=\begin{bmatrix}x_h\\y_h\end{bmatrix}=\begin{bmatrix}\mathbf{x}_h\\\mathbf{z}_h\end{bmatrix}\begin{bmatrix}x&y&f\end{bmatrix}^T,\frac{x_h}{x'_h}=\frac{\tan\alpha}{\tan\xi},y'_h=y_h\qquad(4)$$

Let s be an arbitrary scale factor. Whereas there is an equivalent collinearity relationship of $x'_h/y'_h=X_h/Y_h$ on POR, the relationship between the point $\mathbf{P}_w$ in the planar target coordinate system and its image projection on POR can be expressed as

$$\begin{aligned}&s\begin{bmatrix}x'_h\\y'_h\end{bmatrix}=\begin{bmatrix}M_{11}&M_{12}&M_{13}\\M_{21}&M_{22}&M_{32}\end{bmatrix}\begin{bmatrix}r_{11}&r_{12}&t_1\\r_{21}&r_{22}&t_2\\r_{31}&r_{32}&t_3\end{bmatrix}\begin{bmatrix}X_w\\Y_w\\1\end{bmatrix}-\begin{bmatrix}0\\\Delta F\end{bmatrix},\\&\begin{bmatrix}M_{11}&M_{12}&M_{13}\\M_{21}&M_{22}&M_{23}\end{bmatrix}=\begin{bmatrix}\mathbf{m}_0\times(\mathbf{m}_0\times\mathbf{v}_0)\\\mathbf{m}_0\end{bmatrix},[\mathbf{R}\ \mathbf{T}]=\begin{bmatrix}r_{11}&r_{12}&r_{13}&t_1\\r_{21}&r_{22}&r_{23}&t_2\\r_{31}&r_{32}&r_{33}&t_3\end{bmatrix}\end{aligned}\qquad(5)$$

The above equivalent collinearity equation introduce unknown parameter of F, and forms the model of the photogrammetric system with the sphere refraction effects. Let $\mathbf{X}=[r_{11}, r_{12}, r_{21}, r_{22}, r_{31}, r_{32}, t_1, t_2, t_3]^T$, the calibration of relative orientation parameters can be performed with linear matrix equation as follows

$$\begin{bmatrix}A_{i1}&A_{i2}&A_{i3}&A_{i4}&A_{i5}&A_{i6}&A_{i7}&A_{i8}&A_{i9}\end{bmatrix}\mathbf{X}=\begin{bmatrix}B_i\end{bmatrix}\qquad(6)$$

where,

$$\begin{aligned}&A_{i1}=x'_hM_{21}X_w-y'_hM_{11}X_w,A_{i2}=x'_hM_{21}Y_w-y'_hM_{11}Y_w\\&A_{i3}=x'_hM_{22}X_w-y'_hM_{12}X_w,A_{i4}=x'_hM_{22}Y_w-y'_hM_{12}Y_w\\&A_{i5}=x'_hM_{23}X_w-y'_hM_{13}X_w,A_{i6}=x'_hM_{23}Y_w-y'_hM_{13}Y_w\\&A_{i7}=x'_hM_{21}-y'_hM_{11},A_{i8}=x'_hM_{22}-y'_hM_{12},\\&A_{i9}=x'_hM_{23}-y'_hM_{13},B_i=x'_h\Delta F\end{aligned}$$

In addition, $\mathbf{r}_3$ can be recovered with $\mathbf{r}_3=\mathbf{r}_1\times\mathbf{r}_2$, where $\mathbf{r}_i$ denotes the i^{th} column of $\mathbf{R}=[\mathbf{r}_1,\mathbf{r}_2,\mathbf{r}_3]$. Whereas Eq. (6) introduced unknown constant parameters of F, and the search space of F can be attained via a priori knowledge. Hence, **R** and **T** can be solved when an initial estimation of F is given. The calibration process can be performed through iterative optimization within the search space of F by minimizing the projection error. Let $\mathbf{X}$ = [F, **R**, **T**], and H(**X**) is the object function that needs to be minimized

$$\mathrm{H}(\mathbf{X})=\sum_{i=1}^{m}\left\|\mathbf{U}_i-\breve{\mathbf{U}}\left(\mathbf{M}_0,\mathrm{F},R_1,R_2,n,\mathbf{R}_i,\mathbf{T}_i,\mathbf{P}_{wi}\right)\right\|^2 \qquad (7)$$

where, n is refractive index, R_1, R_2 are the external radius and inside radius of sphere cover, $\mathbf{M}_0$ is intrinsic matrix. $\mathbf{U}_i$ is the measured value of pixel coordinates, F is the distance from the camera center to the sphere center, $\breve{\mathbf{U}}$ is the projection point of $\mathbf{P}_{Wi}$ in image plane, m is the number of image points.

Numerical simulation was performed to evaluate our method under the influence of d, F and standard pixel deviations σ. We simulated an 8×11 array checkerboard target with the grid size of 30 mm ×30 mm. The simulated camera has f_u=f_v=1333 pixels, u_0= 640, v_0= 480, and the sphere cover has R_1=35 mm and n=1.49. The simulation were with **T** = [0, 0, 1500], **R**= [0, 0, 0] and $\mathbf{m}_0$= [0.041, 0.040, 0.998]. Fig. 3 shows the root-mean-square of pixel deviation (RMSE) versus different d and F with and without refraction compensation. The larger d and F, the stronger the pixel distortion, and the pixel distortion were remarkably reduced when calibrated with our algorithm. In particular when d=5mm and F=30mm, the RMSE without compensation can up to 12.44 pixels while the RMSE with compensation was down to 1.11 pixel. Fig. 4 shows the pixel distortion degree under different σ. The results shows that proposed methods were robustness to noise. Fig. 3 and Fig .4 also gives the comparison of distortion distribution when d=5mm.

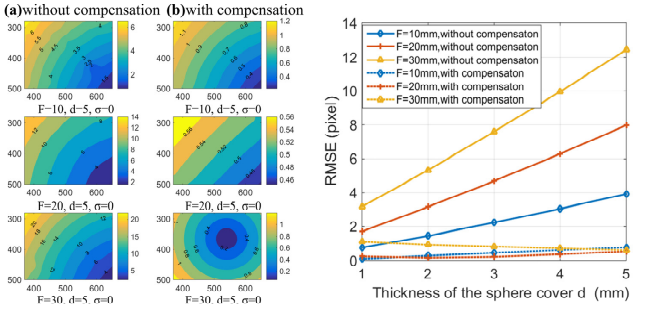

Fig. 3. Simulated image distortion with sphere refraction and compensated image distortion versus F and d.

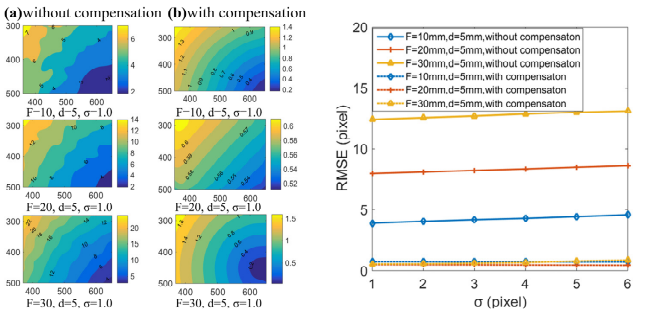

Fig. 4. Simulated image distortion with sphere refraction and compensated image distortion versus standard deviation σ.

In order to further verify the proposed methods, a refractive calibration platform as shown in Fig. 5 was built up, which consists of a camera (MV_EM130M) with resolution of 1280×960 pixels, an 8×11 array checkerboard (AFT-MCT-OV430) with grid size of 30 × 30 mm, a translation stage, and an optical sphere cover with R_1=35mm, d=5mm and n=1.49. The camera were well calibrated by Zhang's method [5] when without cover. The camera intrinsic parameters are: f_x= f_y= 1329 pixels, u_0= 624.4, v_0= 478.3, k_1=-0.086, k_2=0.028, p_1=-0.005, p_2=0.002. The checkerboard was fixed on a mechanical arm that can rotate around the Y-axis of the rotary joint OXYZ as illustrated in Fig. 5(c). The checkerboard images were collected from 25 different positions with and without the optical sphere cover, respectively. The image collected with the sphere cover were then calibrated using our algorithm. The proposed method's performance is compared to the Zhang's algorithm [5], which uses central approximation model with lens distortion considered. We refer it as central approximation (CA) in the following analysis. In each position, the images collected without the sphere cover were used to obtain the ground truth.

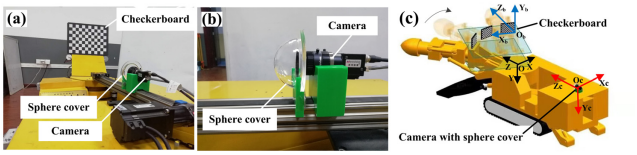

Fig. 5. (a) experiment platform, (b) camera with optical sphere cover, (c) schematic of target trajectory.

Fig. 6 shows the comparison results between ground truth (GT), our algorithm (Ours) and central approximation (CA). Fig. 6(a) shows that the trajectory computed with our algorithm was closer to the actual trajectory. Fig. 6(b) gives the computed F correspond to 25 different positions, it varied from 27.42mm to 32.06mm. It can be observed from Fig. 6(c), (d), (e), (f), (g), and (h) that, by using central approximation, the mean relative error of position were 15.54% in X-axis, 8.16% in Y-axis, and 4.77% in Z-axis, respectively. The mean absolute error of θ_x, θ_y and θ_z were 1.30°, 0.94° and 0.00°, respectively. While by using our algorithm, the mean relative error of position were 2.23% in X-axis, 0.51% in Y-axis, and 0.14% in Z-axis, respectively. The mean absolute error of θ_x, θ_y and θ_z were 0.02°, 0.03° and 0.00°, respectively.

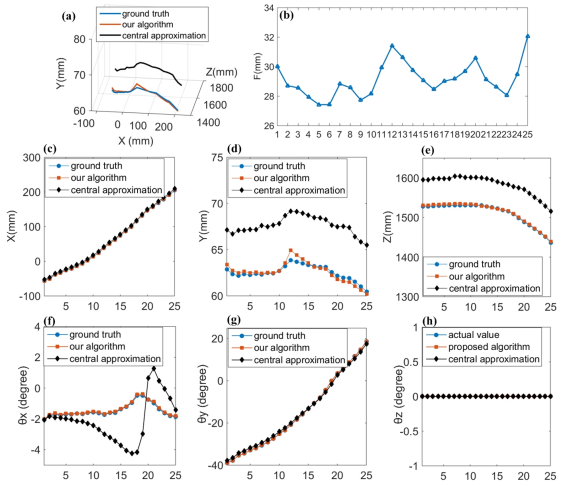

Fig. 6. (a)the comparison results of trajectory tracking; (b) the distance of F at 25 different positions; (c),(d),(e), the position X, Y, and Z in X-

axis, Y-axis and Z-axis, respectively; (f),(g),(h), the rotation angle θ_x, θ_y, and θ_z around X-axis, Y-axis and Z-axis, respectively.

Based on the above calibration results in position 5, 10 and 21, we computed the projected image points of the 8×11 array 3D points. It can be seen from Fig. 7(a) that, in comparison with central approximation algorithm, the projected points were much closer to the actual image points using the proposed algorithm. Moreover, it can be observed from Fig. 7(c) that the mean projection error with central approximation were 1.87 pixel, 1.15 pixel and 1.58 pixel, respectively. The mean projection error using our algorithm were 0.42 pixel, 0.29 pixel and 0.64 pixel. Fig. 7(b) also confirmed that it was consistent in size and direction between the measured image residuals distribution and the projected image residuals distribution using our algorithm.

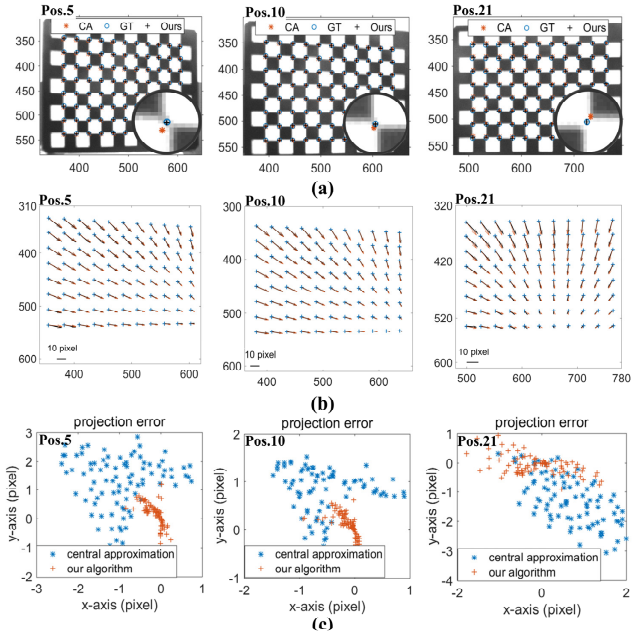

Fig. 7. From left to right were the processed results correspond to position 5, 10 and 21, respectively. (a) The projected image points using CA, Ours and GT. (b) Image residuals distribution triggered by sphere refraction. The blue cross represents the measured image points without the sphere cover, the black arrow represents the measured image residuals, and the red arrow represents the projected image residuals using our algorithm. (c) projection error.

The calibrated relative orientation of checkerboard can also be used to obtain the rectified image points. Fig. 8 shows that the rectified image distortion degree using our algorithm were remarkably reduced in comparison with the actual image distortion, and spherical refraction were well compensated. The actual image distortion distribution triggered by sphere refraction were obtained by the image points measured with and without the optical sphere cover. The root-mean-square of pixel deviation (RMSE) of the unrectified images were 11.25 pixel, 10.72 pixel and 8.08 pixel, respectively. The RMSE of rectified images using our algorithms were 0.81 pixel, 0.69 pixel and 1.14 pixel, respectively. The RMSE of rectified images using CA were respectively 11.33 pixel, 10.78 pixel and 7.49 pixel, which has little effect on the spherical refraction rectification.

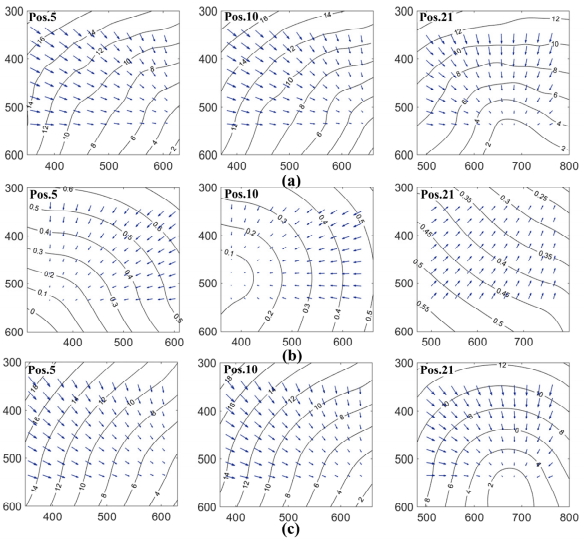

Fig. 8. From left to right were the processed results correspond to position 5, 10 and 21. (a)The distortion distribution of the unrectified images, (b)The distortion distribution of the rectified images using Ours, (c)The distortion distribution of the rectified images using CA.

In summary, an effective model was developed in coplanarity constraint to calibrate the underground camera with spherical refraction effects. Numerical simulation and experiment results demonstrated that the refraction error can be well compensated, and the relative orientation parameters can be well estimated through the proposed method. This method can not only be used to underground camera in coal mine, but also can be extended to other occasions where precision measurement are needed when using photogrammetric systems with optical sphere cover.

Funding. National Natural Science Foundation of China (NSFC) (51974228); National Green Manufacturing System Integration (2017-327), Key R & D project in Shaanxi (2018ZDCXL-GY-06-04)

Acknowledgment. Authors acknowledge the support from the students Yonggang Du, Qifeng, Sheng, Kaixin Zhang, and Chuang Zhou for their assistance in the experiments.

References

1. Y. Wang, Y. Wang, L. Liu, and X. Chen, Opt. Lett. 44, 3254 (2019)
2. Lei HUANG, Qican Zhang, Anand Asundi, Opt. Lett. 38,1446 (2013)
3. Carsten Steger, International Journal of Computer Vision,123,121(2017)
4. R.Y. TSAI, In CVPR, 1986, p.364
5. Z. Zhang, Pattern Anal. Mach. Intell. IEEE Trans. 22, 1330 (2000)
6. R. Hartley and S. B. Kang, In PAMI, 29, 2007.
7. Hou W L, Woods S, Jarosz E, et al. Applied Optics, 51, 2678(2012).
8. Xida Chen, Yee-Hong Yang, In CVPR, 2014.
9. Y. Chang and T. Chen, In ICCV, 2011.
10. C. Kunz and H. Singh, In OCEANS, 2008.
11. L. Kang, L. Wu, and Y.-H. Yang, Applied Optics, 51, 7591(2012).
12. J.-M. Lavest, G. Rives, and J.-T. Lapreste, In ECCV, 2000. p. 654
13. T. Treibitz, Y. Y. Schechner, and H. Singh, In CVPR, 2008.
14. A. Jordt-Sedlazeck and R. Koch, In ICCV, 2013, p. 57
15. Wichmann Verlag, Karlsruhe. Gili Telem, Sagi Filin, ISPRS, 65, 2010
16. Gili Telem, Sagi Filin, ISPRS, 86, 2013.
17. A. Agrawal, S. Ramalingam, Y. Taguchi and V. Chari, In CVPR, 2012.
18. T. Yau, M. Gong, and Y.-H. Yang, In CVPR, 2013.
19. L. Kang, L. Wu, Y. Wei, S. Lao, Y.-H. Yang, Pattern Recognition, 69, (2017)

REFERENCES

1. Yuwei Wang, Yajun Wang, Lu Liu, and Xiangcheng Chen. Defocused camera calibration with a conventional periodic target based on Fourier transform. July 2019, Optics Letters, 44(13):3254.
2. Lei HUANG, Qican Zhang, Anand Asundi. Camera calibration with active phase target: Improvement on feature detection and optimization. May 2013, Optics Letters, 38(9):1446-8
3. Carsten Steger, A Comprehensive and Versatile Camera Model for Cameras with Tilt Lenses, International Journal of Computer Vision 123(2):121-159, 2017
4. R.Y. TSAI, An efficient and accurate camera calibration technique for 3D machine vision, in: Proc. ieee Conf. on Computer Vision & Pattern Recognition, 1986, pp.364–374.
5. Z. Zhang, A flexible new technique for camera calibration, Pattern Anal. Mach. Intell. IEEE Trans. 22 (11) (2000) 1330–1334.
6. R. Hartley and S. B. Kang, "Parameter-Free Radial Distortion Correction with Center of Distortion Estimation," in IEEE Transactions on Pattern Analysis and Machine Intelligence, vol. 29, no. 8, pp. 1309-1321, Aug. 2007.
7. Weilin Hou, Sarah Woods, Ewa Jarosz, Wesley Goode, Alan Weidemann, Optical turbulence on underwater image degradation in natural environments. Applied Optics, 51, 2678-86(2012).
8. Xida Chen, Yee-Hong Yang, Two-View Camera Housing Parameters Calibration for Multi-layer Flat Refractive Interface, Conference: 2014 IEEE Conference on Computer Vision and Pattern Recognition (CVPR), June 2014.
9. Y. Chang and T. Chen. Multi-view 3D reconstruction for scenes under the refractive plane with known vertical direction. In ICCV, 2011.
10. C. Kunz and H. Singh. Hemispherical refraction and camera calibration in underwater vision. In OCEANS, 2008.
11. L. Kang, L. Wu, and Y.-H. Yang. Experimental study of the influence of refraction on underwater three-dimensional reconstruction using the SVP camera model. Applied Optics, 51(31):7591–7603, 2012.
12. J.-M. Lavest, G. Rives, and J.-T. Lapreste. Underwater camera calibration. In ECCV, pages 654–668, 2000.
13. T. Treibitz, Y. Y. Schechner, and H. Singh. Flat refractive geometry. In CVPR, 2008. 1, 2, 7
14. A. Jordt-Sedlazeck and R. Koch. Refractive structure-from-motion on underwater images. In ICCV, pages 57–64, 2013.
15. Wichmann Verlag, Karlsruhe. Gili Telem, Sagi Filin, Photogrammetric modeling of underwater environments, ISPRS Journal of Photogrammetry and Remote Sensing, Volume 65, Issue 5, September 2010, Pages 433-444
16. Gili Telem, Sagi Filin, Photogrammetric modeling of the relative orientation in underwater environments, ISPRS Journal of Photogrammetry and Remote Sensing, Volume 86, December 2013, Pages 150-156
17. A. Agrawal, S. Ramalingam, Y. Taguchi and V. Chari, "A theory of multi-layer flat refractive geometry," 2012 IEEE Conference on Computer Vision and Pattern Recognition, Providence, RI, 2012, pp. 3346-3353.
18. T. Yau, M. Gong, and Y.-H. Yang. Underwater camera calibration using wavelength triangulation. In CVPR, 2013.
19. Lai Kang, Lingda Wu, Yingmei Wei, Songyang Lao, Yee-Hong Yang, Two-view underwater 3D reconstruction for cameras with unknown poses under flat refractive interfaces, Pattern Recognition, Volume 69,2017.